

# Role of Weber number in primary breakup of turbulent liquid jets in crossflow

By M. G. Pai, I. Bermejo-Moreno, O. Desjardins<sup>†</sup> AND H. Pitsch

## 1. Motivation and objectives

Atomization of liquid fuel controls combustion efficiency and pollutant emissions of internal combustion engines and gas turbines (Lefebvre 1998). The liquid jet in crossflow (LJCF) finds application in lean premixed prevaporized (LPP) ducts, afterburners for gas turbines, and combustors for ramjets and scramjets. This flow configuration, which consists of a turbulent liquid jet injected transversely into a gaseous laminar or turbulent crossflow, has been the focus of several experimental studies with the primary objective of proposing scaling laws and regime diagrams for liquid breakup (Sallam *et al.* 2004; Lee *et al.* 2007; Bellofiore, A. 2006). A typical turbulent LJCF exhibits a Kelvin-Helmholtz-type instability wave on the windward side of the liquid column (see schematic in Fig. 1). These waves travel along the liquid column and ultimately lead to its breakup around the time the liquid jet reaches the maximum penetration in the transverse direction. For high crossflow Weber number and momentum flux ratios, a turbulent liquid jet with a circular cross-section gradually changes into an almost crescent shape. Ligaments, drops, and other liquid structures, which are termed dispersed phase elements (DPEs) in the rest of this brief, are shed along the sides of the liquid column especially along the crescent edges. The shedding of DPEs is more prominent at the location of the traveling waves and might be a primary source of DPE production in the LJCF. Primary breakup in the context of a LJCF refers to this first stage of liquid jet breakup, which involves the shedding of DPEs from the liquid column owing to various processes inside the liquid jet and the ambient gas. In the primary breakup stage, DPEs that are shed from the liquid column need not be spherical in shape (see Fig. 1). Depending on the size and velocity of the DPEs (as characterized, say, by the Weber number and Reynolds number corresponding to these structures) that are shed from the liquid column as a result of primary breakup, these DPEs undergo further breakup. This second stage of breakup is termed secondary breakup. Experiments report the drop size distribution that results after primary and secondary breakup, in addition to coalescence of drops and ligaments further downstream, and possibly other sources of drop formation (for instance, satellite drop formation as a result of rebounding drops). Thus a primary breakup model for the LJCF must be able to capture the size distribution (or more precisely, the volume distribution) and possibly other geometrical features of the DPEs immediately after being shed from the liquid column in order to be predictive. This information would be supplied to a secondary breakup model, which then predicts a drop size distribution that can be employed in numerical calculations of multiphase reactive flows with sprays.

Several experiments have shed light on various regimes of breakup and scaling laws for various statistics such as liquid jet penetration and trajectory, Sauter mean diameter of drops and wavelength of liquid surface instabilities have been proposed. Yet,

<sup>†</sup> Department of Mechanical Engineering, University of Colorado, Boulder, Colorado, USA.

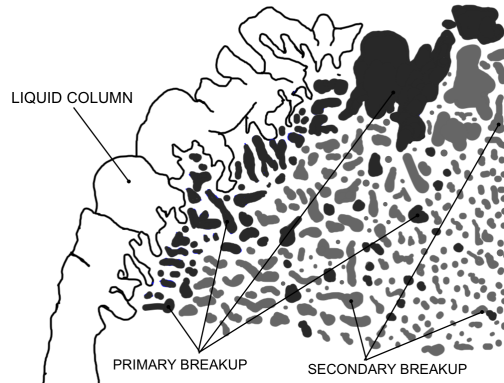


FIGURE 1. Schematic of a turbulent liquid jet in crossflow illustrating a typical breakup scenario. Large liquid structures, ligaments and drops that have just broken off the liquid column and classified to be part of the primary breakup regime are shown in dark grey. Ligaments and drops shown in light grey constitute the secondary breakup regime.

predictive models for primary breakup of turbulent LJCF are still unavailable. Using experiments, it is challenging to perform detailed parametric studies of a LJCF by varying one dimensionless group while fixing the remaining dimensionless groups. However, simple changes of parameters do not pose a challenge to numerical studies. In a recent numerical study (Pai *et al.* 2008, 2009), we demonstrated that the liquid Weber number, rather than the crossflow Weber number, controls the wavelength of liquid surface instabilities on the windward side of the LJCF. This was seemingly in contradiction with a scaling that was proposed using experimental datasets (Sallam *et al.* 2004). On careful interpretation of the experimental dataset however, this seeming contradiction was resolved (see Pai *et al.* 2009 for details) and, interestingly, the experimental observations were in accord with the numerical results. That study underscored the importance of carefully interpreting scaling laws obtained from experiments before using such scaling laws to build primary breakup models.

In the earlier numerical study (Pai *et al.* 2009), the focus was on liquid structures corresponding to the LJCF whose size was on the order of the injector diameter. The assumption was that such structures would be resolved well by the grid and that neglecting the smaller unresolved liquid and gas-phase structures would not affect the large scale structures. In this study, we perform a subset of the simulations from the previous parametric study at the mesh resolution that is necessary to resolve the smallest length scales in the problem. In addition, we investigate the geometrical characteristics of the DPEs that separate from the liquid column using concepts from differential geometry, details of which are provided below.

We begin by reviewing the governing equations for the primary breakup of liquid jets. The scope of the current study is reviewed followed by a discussion on some of the computational details. A discussion of results obtained from the parametric study and the geometrical analysis is presented next. The study concludes with a summary of the principal results and an outlook for future studies.

## 2. Governing equations

We assume constant thermodynamic properties of the liquid and gas phases and use the incompressible Navier-Stokes (NS) equations to describe the problem of liquid breakup:

$$\frac{\partial \mathbf{u}}{\partial t} + \mathbf{u} \cdot \nabla \mathbf{u} = -\frac{1}{\rho} \nabla p + \frac{1}{\rho} \nabla \cdot (\mu (\nabla \mathbf{u} + (\nabla \mathbf{u})^T)), \quad (2.1)$$

where  $\mathbf{u}$  is the velocity,  $p$  is the pressure,  $\rho$  is the thermodynamic density, and  $\mu$  is the dynamic viscosity. The continuity equation

$$\frac{\partial \rho}{\partial t} + \nabla \cdot \rho \mathbf{u} = 0 \quad (2.2)$$

and the incompressibility constraint  $D\rho/Dt = 0$  imply that the velocity field is solenoidal. If  $\Gamma$  represents the interface that separates the two immiscible fluids or phases, then the following condition holds at the interface:

$$[p]_{\Gamma} = \sigma \kappa + \left[ \mu \left( \frac{\partial u_i}{\partial x_j} + \frac{\partial u_j}{\partial x_i} \right) n_i n_j \right]_{\Gamma} \quad (2.3)$$

where  $[Q]_{\Gamma} = Q_+ - Q_-$  represents the jump of a quantity  $Q$ , which has values  $Q_+$  and  $Q_-$  on either side of the interface,  $\kappa$  is the mean curvature,  $\sigma$  is the interfacial tension, and  $\mathbf{n}$  is the unit normal to the interface. We denote the (+) side to be in the liquid (liq) and the (-) side to be in the gas (g). The jump condition in Eq. (2.3) can be simplified to (Kang *et al.* 2000)

$$[p]_{\Gamma} = \sigma \kappa + 2 [\mu]_{\Gamma} \frac{\partial u_i}{\partial x_j} n_i n_j, \quad (2.4)$$

where  $[\mu]_{\Gamma}$  is a constant non-zero jump in the viscosity across the interface. Since the two fluids have different densities, there is a jump in the density, i.e.,  $[\rho]_{\Gamma} = \text{constant}$  across the interface (we assume constant viscosity and density in the two fluids). From the conservation of mass, it follows that for a flow with no interphase mass transfer, the velocity at the interface is continuous, i.e.,  $[\mathbf{u}]_{\Gamma} = 0$ .

A simple analysis of the dimensional quantities that characterize the LJCF reveals that from among the seven non-dimensional groups that characterize the LJCF, which are crossflow Weber number, liquid Weber number, liquid-gas density ratio, momentum flux ratio, liquid Reynolds number, cross-flow Reynolds number, and Ohnesorge number, only five are independent (see Pai *et al.* 2009 for more details).

## 3. Scope of current study

Although the primary purpose of this study is to understand the implications of higher mesh resolution on the liquid jet breakup, the present work also investigates the geometrical characteristics of the DPEs that result from the shedding of ligaments and drops in the domain. From the perspective of primary breakup modeling, it is necessary to quantify the geometrical characteristics of DPEs immediately after being shed from the liquid column. However, in this preliminary study, we focus on the geometrical characteristics of the DPEs in the entire computational domain at a certain characteristic timescale.

From among the five non-dimensional groups that characterize the LJCF, we investigate the role of liquid Weber number and crossflow Weber number in the primary breakup of a liquid jet in crossflow. The liquid Weber number characterizes the tendency of the liquid jet to break up owing to a competition between liquid inertia and surface tension

forces, whereas the crossflow Weber number characterizes the tendency of the liquid jet to break up owing to a competition between the gas-phase inertia and surface tension forces.

## 4. Computational details

### 4.1. Numerical methodology

In this study, a spectrally refined interface tracking scheme for the level set function is employed (Desjardins & Pitsch 2009). This interface tracking technique has several advantages over other available methods such as the volume of fluid (VOF) (Scardovelli & Zaleski 1999), coupled level set/volume of fluid (CLSVOF) (Sussman *et al.* 2007), and Lagrangian particle-based methods (Hieber & Koumoutsakos 2005). See Desjardins (2008) for a detailed discussion. In SRI, the level set field is represented on a finite number of subcell quadrature nodes around the interface. The level set field is advected using a semi-Lagrangian approach, which takes advantage of the fact that the level set equation given by

$$\frac{\partial G}{\partial t} + \mathbf{u} \cdot \nabla G = \frac{DG}{Dt} = 0, \quad (4.1)$$

where  $G(\mathbf{x}, t)$  is the level set field, is a constant along the trajectory of material points moving at velocity  $\mathbf{u}$ . At the new location  $\mathbf{x}^{n+1}$  and time  $t^{n+1}$ , the value of the level set function corresponding to each quadrature node is computed by integrating backward in time to the previous position  $\mathbf{x}^n$  at  $t^n$  along the material point trajectory that passes through  $\mathbf{x}^{n+1}$ . The value of  $G^{n+1}(\mathbf{x}^{n+1})$  is then set equal to  $G^n$  at location  $\mathbf{x}^n$ . As high-order schemes can be used to numerically integrate along the material point trajectory, numerical diffusion of the interface is minimal. This method, in conjunction with the subcell resolution, allows for retaining sharp features of the interface as the liquid jet evolves in time (see Desjardins & Pitsch 2009; Pai *et al.* 2009 for details).

A high-order conservative finite difference scheme (Desjardins *et al.* 2008*a*) is built into an in-house code called NGA, which has been efficiently written with MPI libraries for large-scale distributed memory computations. The variables are staggered in space and time, and centered finite difference schemes are employed. Accurate jump conditions for the pressure given by Eq. (2.4) that include the surface tension force are imposed using a ghost fluid (GF) method (Desjardins *et al.* 2008*b*). Only second-order accuracy will be employed here as the formal order of accuracy is limited by the interfacial GF treatment, which is currently first-order. In order to allow for an implicit treatment of the viscous terms in the NS equations in conjunction with an approximate factorization technique, we adopt a continuous surface force (CSF) formulation for the viscosity. This essentially removes the jump in viscosity in Eq. (2.4) and thus the pressure jump contains only the surface tension.

### 4.2. Computational expense

Resolution requirements for the LJCF are dictated by the need to resolve the smallest length scales in the gas phase and liquid phase, which are primarily governed by the Reynolds number corresponding to each phase, and the smallest structures formed during liquid breakup, which are primarily governed by the liquid and crossflow Weber number.

We use a turbulent pipe flow for the liquid injection, so the smallest length scales in the liquid jet are governed by the liquid Reynolds number based on injector diameter  $d$ ,  $Re_{\text{liq}} = \rho_l U_{\text{liq}} d / \mu_{\text{liq}}$ . Assuming a uniform mesh resolution  $\Delta x = 2\delta_v$ , where  $\delta_v$  is the

viscous length scale in the turbulent pipe flow, we obtain a scaling for the number of points along the injector diameter  $N_{\text{dia}} = d/\Delta x$  with  $Re_{\text{liq}}$  as (see Pai *et al.* 2009 for details)

$$N_{\text{dia}} = 0.1 Re_{\text{liq}}^{7/8}. \quad (4.2)$$

For droplet-laden flows, the liquid Weber number decides the competitive effects of inertia and surface tension forces and thus the likelihood of a drop to undergo further breakup. Theoretical analyses (Hinze 1955) and experiments (Lefebvre 1998) suggest that drops with liquid Weber number less than  $\sim 10$  normally do not undergo further breakup. The need to resolve droplets (or liquid structures) until this limit imposes a requirement on the smallest grid size in the computational domain. In other words, we require that the Weber number based on the grid size  $\Delta x$ ,  $We_{\Delta x}$ , be less than 10, i.e.,  $We_{\Delta x} = \rho_l U_l^2 \Delta x / \sigma < 10$  from which a criterion on  $N_{\text{dia}}$  arises as

$$N_{\text{dia}} > 0.1 We_{\text{liq}}. \quad (4.3)$$

For the cases considered here, the crossflow Weber number ( $We_{\text{cf}}$ ) based on the injector diameter is less than the liquid Weber number ( $We_{\text{liq}}$ ), so the above requirement for  $N_{\text{dia}}$  based on  $We_{\text{liq}}$  is more restrictive.

From the foregoing analysis, an estimate for the grid size required in the entire computational domain is

$$N_{\text{tot}E} = (C_{xb} + n_{xb})(C_{yb} + n_{yb})n_z q^{1/2} \max(0.001 We_{\text{liq}}^3 / r^3, 0.001 Re_{\text{liq}}^{21/8}), \quad (4.4)$$

where  $n_{xb} = 3$  and  $n_{yb} = 4$  account for an additional buffer region upstream of the injector inlet for the flow to develop around the liquid column, and along the  $y$  direction, respectively. Also,  $r + 1$  is the number of quadrature nodes in each cell (see discussion below). Note that since this estimate is obtained by using a uniform grid everywhere in the computational domain, it can be considered as an upper bound on the grid size.

Liquid structures smaller than the flow solver (velocity-pressure) cell can potentially be retained as the SRI method provides subcell resolution Desjardins & Pitsch (2009). One may resolve up to  $r$  times larger Weber numbers by adopting the subcell resolution compared to that resolved on the flow solver grid. Although this is the case, we use  $r = 2$  in the current study. This essentially implies that a flow solver cell has 27 quadrature nodes with one of these nodes at the cell center. The primary reason for employing  $r = 2$  rather than  $r = 4$  as in Pai *et al.* (2009) is the significant computational expense in terms of memory that one incurs with increasing  $r$ , especially when the flow solver resolution is itself very high (see Table 1). For instance,  $r = 2$  implies 27 additional memory locations, whereas  $r = 4$  implies 125 additional memory locations to retain information on the sub-cell  $G$  field in each flow solver cell. For instance, if there are 200,000 flow solver cells on each process in a parallel computing environment, and assuming that 25% of these cells have subcell resolution due to the presence of the interface, the overhead is around 1 million additional memory locations for  $r = 2$  and 6 million additional memory locations for  $r = 4$ . Especially at high Weber number  $We_{\text{liq}} > 500$ , there are regions in the computational domain where all the 200,000 flow solver cells have subcell resolution. Load balancing under these circumstances becomes an enormous challenge, especially for the inhomogeneous geometry that is under consideration and the uniform domain decomposition adopted in this study. Incorporating an efficient, adaptive load balancing technique in the context of the SRI methodology is left as a future exercise.

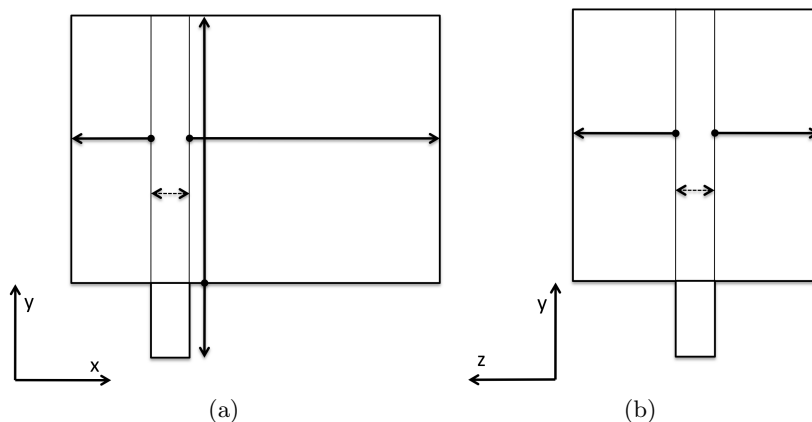


FIGURE 2. Schematic views of the computational domain (not drawn to scale) used in the current study. The solid arrows denote the part of the domain where geometric mesh stretching is employed, whereas the arrow head indicates the direction of increasing mesh size. Dashed arrow denote regions where a uniform mesh is employed.

#### 4.3. Computational domain

Figure 2 shows a schematic of the computational domain typically used for the cases considered in this study. An injector length of  $L_d = 2d$  is employed to capture the interactions between the crossflow and the liquid jet at the injection point. A turbulent pipe inflow at the required Reynolds number is injected at the entrance of the injector. The crossflow is located three diameters upstream of the injector location. Along the direction of the crossflow, the total length of the domain is equal to  $12d$ , whereas in the transverse  $z$  direction the length of the domain is  $9d$ . Along the  $y$  direction, the length of the domain is different for each case and is presented in Table 1. One reason for the small size of the computational domain compared to that used in Muppidi & Mahesh (2007) is the sheer computational expense incurred to resolve both the gas-phase and liquid scales, with the latter being more restrictive as it has to be resolved over the entire domain. Furthermore, we focus on the region close to the injector and thus restrict ourselves to a small computational domain. For optimum conservation of liquid mass, one prefers a uniform mesh at least in the region of the domain where the liquid jet is expected to be present. However, from Eq. 4.4, the total number of grid points required for a uniform grid can be enormous (see Table 1 for details), which in turn demands several thousands of processors. Even on a machine such as Ranger at TACC, which has over 30,000 processors, it is not practical to perform parametric studies with a uniform grid resolution in a given timeframe. To minimize computational expense, yet resolve the liquid and gas phase length scales close to injection, we adopt a gradual geometric stretching of the mesh, where the  $n$ th mesh size  $\Delta x_n = a\Delta x_{n-1}$  with  $a = 1.005$  (see Fig. 2).

## 5. Results and discussion

### 5.1. Parametric study

We choose a subset of the parametric study presented in Pai *et al.* (2009) as the focus of the current study. Table 1 provides a description of the various test cases. Cases (a) and (b) correspond to constant  $We_{liq}$  for varying  $We_{cf}$ , whereas cases (a) and (c)

Cases	$q$	$We_{cf}$	$We_{liq}$	$Re_{liq}$	$N_{dia}$	$N_{tot}$ (actual)	$L_x, L_y, L_z$ (times $d$ )	$N_{proc}$	$N_{tot E}$ (Eq. 4.4)
(a)	5	100	500	5000	172	334 million	(12, 12, 8)	2048	~2.2 billion
(b)	10	50	500	5000	172	334 million	(12, 12, 8)	2048	~2.2 billion
(c)	10	100	1000	5000	172	334 million	(12, 12, 8)	2048	~2.2 billion
(d)	5	100	500	7500	245	518 million	(12, 16, 7)	3136	~5 billion
(e)	30	100	3000	5000	172	324 million	(12, 20, 6)	2112	~3.6 billion

TABLE 1. Parameters of the test cases for varying momentum flux ratios, crossflow Weber number and liquid Weber numbers. Grid dimensions are  $(660 \times 660 \times 768)$  for cases (a), (b), and (c), and  $(800 \times 720 \times 900)$  and  $(660 \times 768 \times 640)$  for cases (d) and (e), respectively. Crossflow Reynolds number  $Re_{cf} = 1000$  for all cases.  $N_{proc}$ : total number of processors used for each computation. Although results from cases (d) and (e) are available, for the sake of brevity a discussion of these results is not presented in this study.

Case	$q$	$We_{cf}$	$We_{liq}$	$\lambda/d$	$\lambda/d$ (from Pai <i>et al.</i> 2009)
(a)	5	100	500	0.80	0.94
(b)	10	50	500	0.83	(NA)
(c)	10	100	1000	0.7	0.78

TABLE 2. Wavelength of the K-H instability obtained from the current study

correspond to constant  $We_{cf}$  for varying  $We_{liq}$ . Cases (d) and (e) are two additional test cases performed at higher liquid Reynolds number and liquid Weber number, respectively. Results from cases (d) and (e) are not presented here and will be reported in a subsequent study.

### 5.2. Wavelength of liquid surface instabilities

As in the earlier study of Pai *et al.* (2009), we investigate the role of Weber number in determining the wavelength of the liquid surface instability on the windward side of the liquid jet. As explained in Pai *et al.* (2009), a slice is cut through the liquid jet that is parallel to the  $x$ - $y$  plane passing through the injector center. This slice is observed close to the injector and the wavelength of the K-H instability is measured in time. Table 2 provides the wavelength of these instabilities for cases (a), (b) and (c). The simulations in this study have been performed only for one flow through time, therefore the wavelength was averaged over only ten snapshots of liquid jet over that time. Yet the mean values of the wavelengths are in the same range as obtained in the earlier study. More snapshots from the current study are needed to confirm if one can identify a trend with increasing mesh resolution.

### 5.3. Geometrical analysis of structures

Insight into the role of Weber number on ligament and drop formation in the primary breakup regime is obtained by investigating the geometrical characteristics of the ligaments and drops just after separation from the liquid column. A methodology for the study of the geometry of three-dimensional structures was introduced and applied to

single-phase turbulent flows in Bermejo-Moreno & Pullin (2008). In the present study, we consider a subset (namely, the geometrical characterization step) of that methodology to analyze structures educed from instantaneous snapshots of the evolution of turbulent liquid jets in cross flow. Although as noted earlier, the focus of the geometrical characterization should be the ligaments that have just separated from the liquid column, in this study we focus on all the liquid structures that have separated from the liquid column until a certain characteristic time (see below). In this preliminary study, the effect of the physical parameters  $g$ ,  $We_{\text{liq}}$ , and  $We_{\text{cf}}$  on the liquid structure geometry for two different instants in time is reported.

### 5.3.1. Methodology

At every point of a given closed surface with area  $A$  and volume  $V$ , we obtain two differential geometry properties: the absolute value of the shape index  $\tilde{S}$ , and the dimensionless curvedness  $\tilde{C}$  (non-dimensionalized with the lengthscale  $\mu = 3V/A$ ). Then, a joint probability density function of those two variables, based on area coverage throughout the surface, is calculated and its feature center,  $\{S, C\}$ , is obtained. The feature center is a modified mean that accounts for asymmetries of the joint pdf. We also consider the stretching parameter,  $\lambda = \sqrt[3]{36\pi} V^{2/3}/A$ . A brief physical interpretation of these properties is presented next.

Structures with different shapes have a corresponding location in the  $\{S, C, \lambda\}$  three-dimensional space. Blob-like structures, for example, gather near the  $\{1, 1, 1\}$  point (which corresponds to spheres). Tube-like structures are proximal to the  $\{1/2, 1, \lambda\}$  axis. The transition to sheet-like structures occurs for decreasing values of  $C$  and  $\lambda$ . Lower values of  $\lambda$  imply more stretched structures. A complete description of the characterization, as well as the geometrical interpretation of these parameters is given in Bermejo-Moreno & Pullin (2008).

### 5.3.2. Application to structures of liquid jets

For each of the cases (a), (b), and (c), we consider the characteristic time for breakup of the liquid column  $t_b$  given by (Sallam *et al.* 2004)

$$t_b = C_b \sqrt{q} \frac{d}{U_{\text{inj}}},$$

where  $C_b = 2.5$  and  $U_{\text{inj}}$  is the bulk liquid injection velocity, and two instants in time  $t_1 = t_b$  and  $t_2 = 1.4t_b$  (the factor 1.4 is arbitrary and is chosen as we are yet to accumulate results beyond this time).

Table 3 shows the number of broken-up structures for each case. As expected, this number increases with time for the three cases. It is interesting to note that for the cases (a) and (b) which have the same liquid Weber number, the total number of structures is about the same. Note that the  $We_{\text{cf}}$  of case (b) is half that of case (a). Furthermore, the number of structures in case (c) is nearly three times that of case (a), although their  $We_{\text{cf}}$  are the same. One can conclude that at least in this stage of liquid breakup and for the parameters of the simulation, the number of separated structures is controlled by the liquid Weber number.

Figure 3 shows the probability density function of the  $\mu$  parameter of the broken-up structures. This parameter defines a characteristic lengthscale of the structure. For a sphere,  $\mu$  equals its radius, whereas for tubes and sheets,  $\mu_{\text{tube}} \approx 3t/4$  and  $\mu_{\text{sheet}} \approx t/2$ , respectively, where  $t$  is the thickness. Interestingly,  $We_{\text{cf}}$  has a dominant effect on these pdfs. Both cases with  $We_{\text{cf}} = 100$  show similar pdfs for a wide range of  $\mu$  values (they

---

Case	$q$	$We_{cf}$	$We_{liq}$	$N_{struct}(t_1)$	$N_{struct}(t_2)$
(a)	5	100	500	269	586
(b)	10	50	500	276	578
(c)	10	100	1000	787	1426

---

TABLE 3. Number of structures broken up from the liquid jet for each case and at the two instants in time under consideration

---

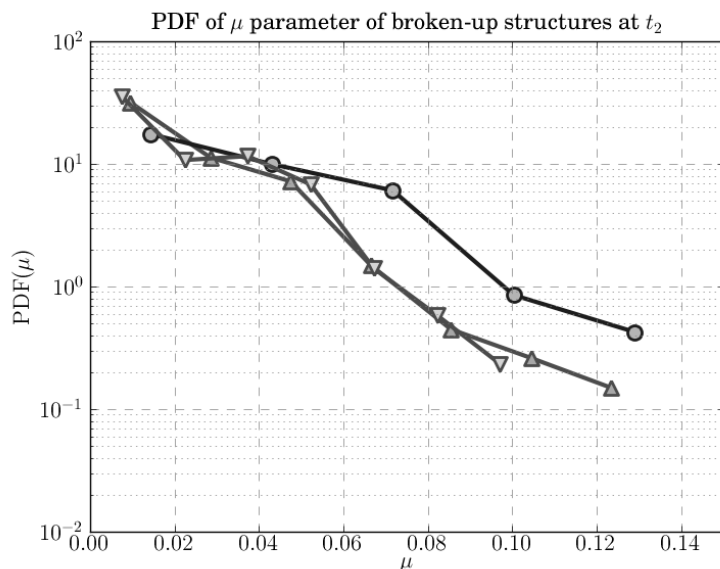


FIGURE 3. Pdf of  $\mu$  parameter for the three cases at  $t_2$ . Triangles: case (a), circles: case (b); inverted triangles: case (c). Points defined at the center of intervals.

still differ in the right tail), whereas the case with  $We_{cf} = 50$  tends to have comparatively higher values of the  $\mu$  lengthscale. The result datasets suggest that the crossflow Weber number controls the characteristic thickness of the liquid structures in this parameter range.

Figure 4 contains plots of the  $\{S, C, \lambda\}$  space representing the geometry of broken-up structures for each case and time. Each point in that plot corresponds to one broken-up structure. The size of each point is scaled with the  $\mu$  parameter of its corresponding structure. Figure 5 shows projections of that space on the  $S - C$  plane. The location of prototypical shapes (blobs, tubes and sheets), as explained in Sec. 5.3.1, is also included in those plots for reference. With regard to the geometrical features of each case, it is observed that blob-like geometry is predominant among the structures broken up from the liquid jet. An increase of blob-like structures is observed for the three cases at later time which could be attributed to new structures breaking up from the jet or from secondary breakup of the structures at earlier time. The trend observed in Table 3 is reflected in how populated the distributions of points are in Fig. 5, whereas the effect of the scaling of the points by  $\mu$  is directly related to the pdf shown in Fig. 3. We note that the location

of points in the  $\{S, C, \lambda\}$  space contains shape information that is independent of the size of the structure, while the size of each point in that space is related to a lengthscale of the structure, as defined above. The scaling is common to all plots, so that they can be consistently compared. For instance, the presence of larger points in case (b) at  $t_2$  indicates a tendency to higher values of  $\mu$  as plotted in Fig. 3.

Case (c) (bottom panel in Figs. 4 and 5) shows a larger spread of geometrical shapes among the three cases. In particular there are large structures with relatively low values of  $\lambda$  (i.e., considerable stretching). Also the value of  $C$  shows a higher variance, reaching lower values than for the other two cases. The combined effect of lower values of  $\lambda$  and  $C$  reflects a tendency toward sheet-like structures. These are less common for the other two cases. Despite some occurrences of structures approaching the sheet-like region, this type of geometry is not as commonly encountered as blobs, tubes and the other shapes.

## 6. Conclusions and future work

The objective of this study was twofold. One was to ascertain the effect of mesh resolution on the evolution of the LJCF. We notice that the mesh resolution does not affect the wavelength of the liquid surface instabilities lending credence to our assumption in Pai *et al.* (2009) that the coarse mesh resolution does not affect these statistics. The other objective involved using a differential geometry technique to analyze liquid structures for their geometrical characteristics. In the earlier study (Pai *et al.* 2009), we provided evidence that the wavelength of liquid surface instabilities were controlled primarily by the liquid Weber number. We further concluded by observing the liquid mass evolution that the smallest lengthscales of the liquid jet were controlled again by the liquid Weber number. From the preliminary geometrical analysis of liquid structures that was performed in this study, intriguingly however it appears that the role of crossflow Weber number in the primary breakup of the liquid jet cannot be entirely discounted. For the parameters of the study, it appears that the crossflow Weber number controls the characteristic thickness of the liquid structures, while the shapes of the liquid structures, such as blobs, tubes or sheets, are controlled by the liquid Weber number. Yet we observe that the number of liquid structures produced at the same characteristic timescale is controlled by the liquid Weber number. This may point to an interesting mechanism of breakup of ligaments where the inertia in the liquid as characterized by the liquid Weber number causes separated structures to break up further, with the characteristic thickness of these structures being controlled by the crossflow Weber number.

Geometrical analyses such as the one presented in this study seem very appropriate from the purview of primary breakup modeling. The analysis presented in this study suggests that it might not be sufficient for a primary breakup model to merely predict a size distribution of droplets. Such geometrical and statistical analyses using multiple independent simulations of LJCF might reveal that a primary breakup model must capture the presence of a certain proportion of separated structures (such as blobs, tubes and sheets), or model its effect on the size or volume distribution of separated structures that it supplies to a secondary breakup model. Clearly, a primary breakup model that simply provides a distribution of spherical droplets without regard to the subtle processes involved during this stage of breakup cannot be expected to be predictive in realistic simulations of gas-turbine combustors, where unsteadiness in both the liquid jet injection and the crossflow can modify the primary breakup mechanisms. This might in

turn lead to drop size distributions after secondary breakup that can be very different from experimentally measured distributions such as the log-normal distribution.

Ideally the simulations and the analyses presented in this study need to be extended to several tens of diameters downstream from the liquid injection, so that a comprehensive analysis of primary and secondary breakup of liquid jets may be performed. However, the immense computational cost prohibits such detailed numerical simulations from being carried out, at least at present. Such detailed numerical simulations need to be contrasted with simulations that use the large-eddy simulation technique for the carrier phase. Furthermore, in such simulations small separated structures are converted to point particles. While these are attractive techniques to reduce computational expense, they add a level of uncertainty and modeling into the entire breakup process which defeats the very purpose of performing detailed simulations in the first place. Findings from such analyses will in turn depend on modeling parameters (such as the LES sub-grid models for both the liquid and gas phase, the threshold below which a ligament is considered a point particle, etc.) and their effect on primary breakup processes identified in this study will need to be precisely quantified.

Detailed numerical simulations are able to provide unique insight into the mechanism of breakup of a LJCF. Such simulations coupled with careful analyses such as the one presented in this study can unravel intricacies and subtleties in liquid primary breakup, which was until now deemed to be controlled by a single parameter (for instance, the crossflow Weber number is the principal non-dimensional group used in regime diagrams for LJCF).

### Acknowledgments

Funding from UTRC and NASA is acknowledged. Computational time for numerical simulations were made available on TACC-Ranger and TACC-Spur at The University of Texas, Austin, through a NSF compute time grant.

### REFERENCES

- BELLOFIORE, A. 2006 Experimental and numerical study of liquid jets injected in high-density air crossflow. PhD thesis, University of Naples.
- BERMEJO-MORENO, I. & PULLIN, D. I. 2008 On the non-local geometry of turbulence. *J. Fluid Mech.* **603**, 101–135.
- DESJARDINS, O. 2008 Numerical methods for liquid atomization and application in detailed simulations of a diesel jet. PhD thesis, Stanford University.
- DESJARDINS, O., BLANQUART, G., BALARAC, G. & PITSCH, H. 2008*a* High order conservative finite difference scheme for variable density low Mach number turbulent flows. *Journal of Computational Physics* **227** (15), 7125–7159.
- DESJARDINS, O., MOUREAU, V. & PITSCH, H. 2008*b* An accurate conservative level set/ghost fluid method for simulating turbulent atomization. *Journal of Computational Physics* **227** (18), 8395–8416.
- DESJARDINS, O. & PITSCH, H. 2009 A spectrally refined interface approach for simulating multiphase flows. *Journal of Computational Physics* **228** (5), 1658–1677.
- HIEBER, S. & KOUMOUTSAKOS, P. 2005 A Lagrangian particle level set method. *Journal of Computational Physics* **210** (1), 342–367.

- HINZE, J. 1955 Fundamentals of the hydrodynamic mechanism of splitting in dispersion processes. *AIChE Journal* **1** (3), 289–295.
- KANG, M., FEDKIW, R. & LIU, X. 2000 A boundary condition capturing method for multiphase incompressible flow. *Journal of Scientific Computing* **15** (3), 323–360.
- LEE, K., AALBURG, C., DIEZ, F., FAETH, G. & SALLAM, K. 2007 Primary breakup of turbulent round liquid jets in uniform crossflows. *AIAA journal* **45** (8), 1907.
- LEFEBVRE, A. 1998 *Gas turbine combustion*. CRC.
- MUPPIDI, S. & MAHESH, K. 2007 Direct numerical simulation of round turbulent jets in crossflow. *Journal of Fluid Mechanics* **574**, 59–84.
- PAI, M. G., DESJARDINS, O., & PITSCH, H. 2008 Detailed numerical simulations of primary breakup of liquid jets in crossflow. In *Annual Research Briefs*. Center for Turbulence Research.
- PAI, M. G., PITSCH, H. & DESJARDINS, O. 2009 Detailed Numerical Simulations of Primary Atomization of Liquid Jets in Crossflow. In *47th AIAA Aerospace Sciences Meeting*. American Institute of Aeronautics and Astronautics.
- SALLAM, K. A., AALBURG, C. & FAETH, G. 2004 Breakup of round nonturbulent liquid jets in gaseous crossflow. *AIAA journal* **42** (12), 2529–2540.
- SCARDOVELLI, R. & ZALESKI, S. 1999 Direct numerical simulation of free-surface and interfacial flow. *Annual Review of Fluid Mechanics* **31** (1), 567–603.
- SUSSMAN, M., SMITH, K. M., HUSSAINI, M. Y., OHTA, M. & ZHI-WEI, R. 2007 Direct numerical simulation of free-surface and interfacial flow. *J. Comp. Physics* **221**, 469–505.

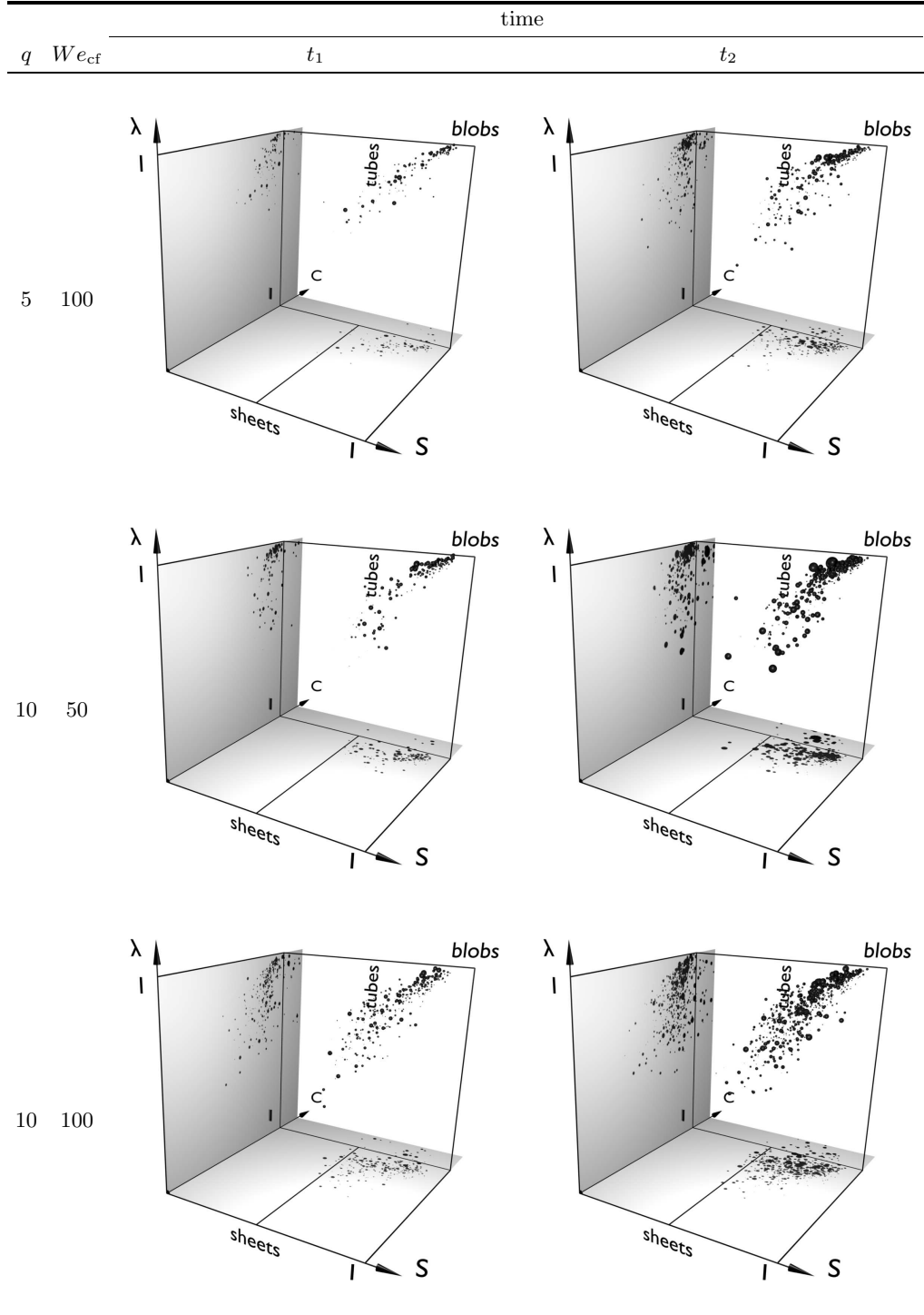


FIGURE 4. Representation of the geometry of individual structures broken up from the liquid jets in the three-dimensional space  $\{S, C, \lambda\}$ . Each point represents one structure. Its size is a measure of the  $\mu$  parameter of the corresponding structure.

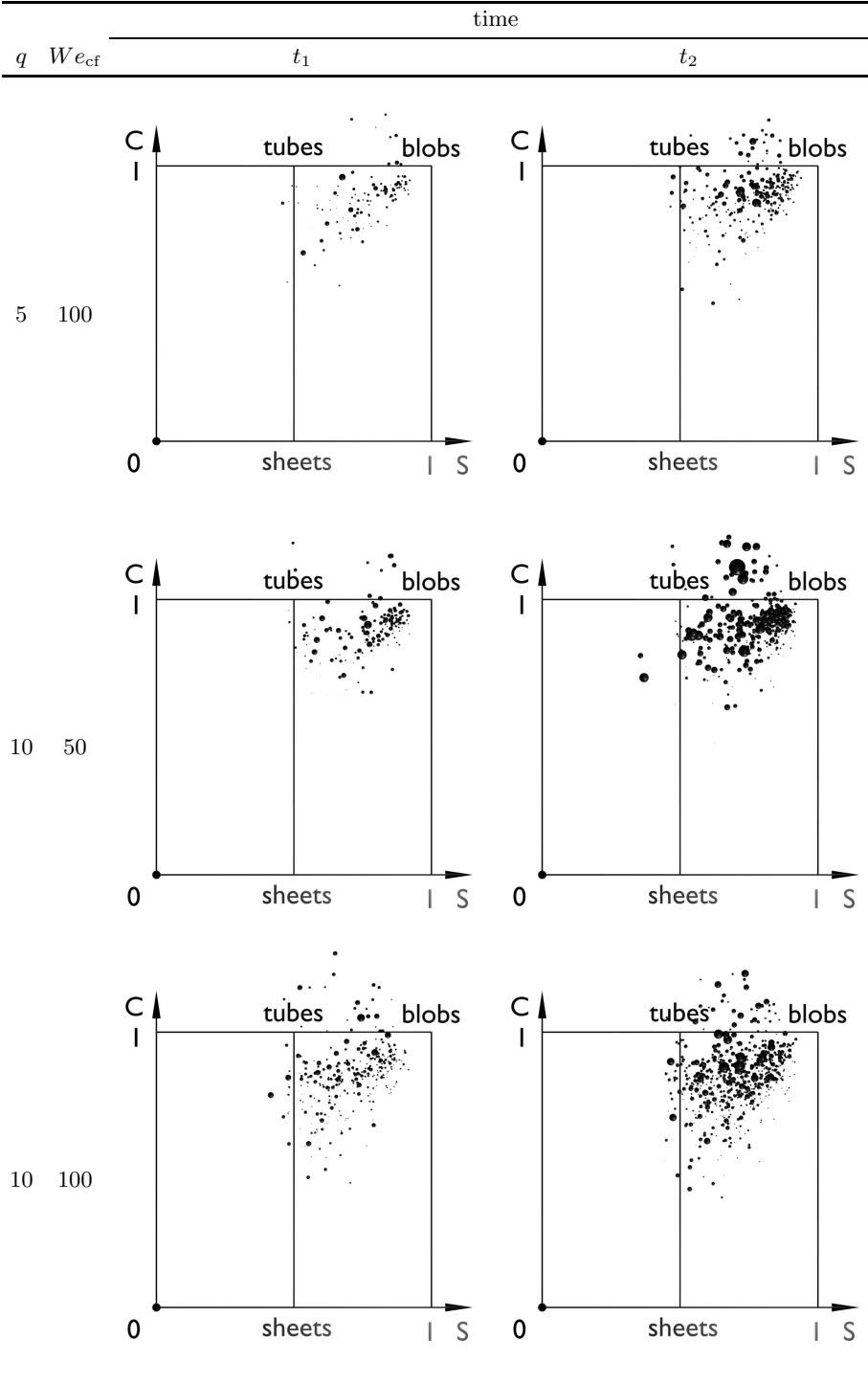


FIGURE 5. Representation of the geometry of individual structures broken up from the liquid jets in the plane  $\{S, C\}$ . Each point represents one structure. Its size is a measure of the  $\mu$  parameter of the corresponding structure.